Density-driven structural transformations in B2O3 glass

ZEIDLER, Anita, WEZKA, Kamil, WHITTAKER, Dean A. J., SALMON, Philip S., BARONI, Axelle, KLOTZ, Stefan, FISCHER, Henry E., WILDING, Martin, BULL, Craig L., TUCKER, Matthew G., SALANNE, Mathieu, FERLAT, Guillaume and MICOULAUT, Matthieu

Published version

ZEIDLER, Anita, WEZKA, Kamil, WHITTAKER, Dean A. J., SALMON, Philip S., BARONI, Axelle, KLOTZ, Stefan, FISCHER, Henry E., WILDING, Martin, BULL, Craig L., TUCKER, Matthew G., SALANNE, Mathieu, FERLAT, Guillaume and MICOULAUT, Matthieu (2014). Density-driven structural transformations in B2O3 glass. Physical Review B, 90 (2), 024206-1-024206-12.

Density-driven structural transformations in B_2O_3 glass

Anita Zeidler,[1] Kamil Wezka,[1] Dean A. J. Whittaker,[1] Philip S. Salmon,[1,*] Axelle Baroni,[2,3,4] Stefan Klotz,[2] Henry E. Fischer,[5] Martin C. Wilding,[6] Craig L. Bull,[7] Matthew G. Tucker,[7] Mathieu Salanne,[3] Guillaume Ferlat,[2,†] and Matthieu Micoulaut[4]

[1]*Department of Physics, University of Bath, Bath BA2 7AY, United Kingdom*
[2]*Sorbonne Universités, UPMC Université Paris 06, UMR 7590, IMPMC, F-75005 Paris, France*
[3]*Sorbonne Universités, UPMC Université Paris 06, UMR 8234, PHENIX, F-75005 Paris, France*
[4]*Sorbonne Universités, UPMC Université Paris 06, UMR 7600, LPTMC, F-75005 Paris, France*
[5]*Institut Laue Langevin, 6 rue Jules Horowitz, Boîte Postale 156, 38042 Grenoble, France*
[6]*Institute of Mathematical and Physical Sciences, Aberystwyth University, Aberystwyth SY23 3BZ, United Kindgom*
[7]*ISIS Facility, Rutherford Appleton Laboratory, Chilton, Didcot, Oxon OX11 0QX, United Kingdom*

(Received 3 July 2014; published 31 July 2014)

The method of *in situ* high-pressure neutron diffraction is used to investigate the structure of B_2O_3 glass on compression in the range from ambient to 17.5(5) GPa. The experimental results are supplemented by molecular dynamics simulations made using a newly developed aspherical ion model. The results tie together those obtained from other experimental techniques to reveal three densification regimes. In the first, BO_3 triangles are the predominant structural motifs as the pressure is increased from ambient to 6.3(5) GPa, but there is an alteration to the intermediate range order which is associated with the dissolution of boroxol rings. In the second, BO_4 motifs replace BO_3 triangles at pressures beyond 6.3 GPa and the dissolution of boroxol rings continues until it is completed at 11–14 GPa. In the third, the B-O coordination number continues to increase with pressure to give a predominantly tetrahedral glass, a process that is completed at a pressure in excess of 22.5 GPa. On recovery of the glass to ambient from a pressure of 8.2 GPa, triangular BO_3 motifs are recovered but, relative to the uncompressed material, there is a change to the intermediate range order. The comparison between experiment and simulation shows that the aspherical ion model is able to provide results of unprecedented accuracy at pressures up to at least 10 GPa.

DOI: 10.1103/PhysRevB.90.024206 PACS number(s): 61.43.Fs, 61.05.F−, 62.50.−p, 64.70.kj

I. INTRODUCTION

B_2O_3 is a prototypical glass-forming oxide material that is an essential component in many industrial glasses [1–48]. Under ambient conditions, the structure of B_2O_3 glass is based on corner-sharing planar BO_3 triangles which link to form a low-density network [2–4,9]: The ambient-pressure and high-pressure crystalline phases of B_2O_3 are ∼41% and 71% more dense than the glass, respectively [49,50]. Three triangular motifs can link to form a planar B_3O_6 boroxol ring, but the fraction f of boron atoms in these rings has been the source of intense debate with estimates ranging from $f = 0$ to $f \gtrsim 0.85$ [5,6,11,19,35,36]. The majority of recent investigations are consistent with a large fraction of boroxol rings, where the precise value may depend on the sample preparation and thermal history. For example, a ^{11}B double rotation nuclear magnetic resonance (NMR) experiment gives $f = 0.73(1)$ [41], as compared to f values of 0.66–0.75 from other ^{11}B NMR experiments [13,18,22,32], $f > 0.67$ from inelastic neutron scattering experiments [20], and $f \sim 0.75$ from an interpretation of Raman spectroscopy and ^{11}B NMR data using first-principles molecular dynamics (MD) simulations [33]. However, it has proved difficult to build atomistic models for B_2O_3 glass with $f \gtrsim 0.2$ that are in quantitative agreement with the measured neutron and x-ray diffraction patterns [16,19,23], although this issue has been addressed in more recent work [37,47] where a first-principles MD model with $f = 0.75$ also accounts for the measured ^{11}B and ^{17}O NMR and Raman spectra [37]. Notwithstanding, the network topology of B_2O_3 is very different to silica and germania where the ambient-pressure structure is based on corner-sharing MO_4 (M = Si or Ge) tetrahedra.

In view of the importance of B_2O_3 as a network-forming oxide, the openness of the glass network under ambient conditions, and the observation that spontaneous crystallization from the melt is obtained only when the pressure is raised above a threshold of ∼0.4–1.0 GPa [51,52], there is considerable interest in the behavior of this material under pressure [1,7,10,15,21,24–32,34,38–40,42–46]. In the case of the glass there is, however, no consensus on the process of network collapse. For example, the x-ray diffraction experiments of Brazhkin *et al.* [39] show that the coordination number of oxygen around boron remains at $\bar{n}_B^O = 3$ as the pressure is increased from ambient to 6.6 GPa and then increases with pressure to give $\bar{n}_B^O = 3.3$ at 9.5 GPa. In comparison, the boron K-edge inelastic x-ray scattering experiments of Lee *et al.* [31] indicate a change in $\bar{n}_B^O$ from 3 to 3.46(5) at a pressure in the range from 4.1 to 7.3 GPa, followed by a steady increase to $\bar{n}_B^O = 3.92(5)$ at a pressure of 22.5 GPa. The B_2O_3 glasses recovered from high pressures to ambient conditions are permanently compacted with an increased refractive index [1,7,10,21,25,32,38,42,45,46,51].

The present work takes advantage of recent developments in high-pressure neutron diffraction as applied to amorphous materials [53–56] to measure the structure of B_2O_3 glass *in situ* at pressures increasing from ambient to 17.5 GPa.

*Corresponding author: p.s.salmon@bath.ac.uk
†Corresponding author: Guillaume.Ferlat@impmc.upmc.fr

It also builds on these developments for reactor source instrumentation by using a shorter incident neutron wavelength of ∼0.5 Å to extend the measured scattering vector Q range, thereby enhancing the real-space resolution of the measured pair-distribution functions. Neutron diffraction offers complementary information to x-ray diffraction on the structure of B_2O_3 glass since it is more sensitive to the boron atom correlations: The relative weighting factors for the B-B, B-O, and O-O correlations are 0.1868:0.4910:0.3225 for neutron diffraction (assuming use of the isotope ^{11}B to avoid the neutron absorption problems related to ^{10}B) versus 0.0865:0.4152:0.4983 for x-ray diffraction at $Q = 0$. The experimental results are compared to those obtained from MD simulations made using an aspherical ion model (AIM) [57,58] that is newly developed for B_2O_3, and which gives a good account of the measured equation of state. It is found that three densification regimes are associated with the pressure-induced transformation of B_2O_3 to a predominantly tetrahedral glass.

The paper is organized as follows. The essential theory for the neutron diffraction experiments is given in Sec. II. The experimental and MD methods are then described in Secs. III and IV, respectively. The results are presented in Sec. V and are discussed in Sec. VI relative to the results obtained from previous high-pressure work. Conclusions are drawn in Sec. VII.

II. THEORY

In a neutron diffraction experiment the total structure factor

$$S_N(Q) = 1 + \frac{1}{\langle b\rangle^2}\sum_{\alpha=1}^{n}\sum_{\beta=1}^{n} c_\alpha c_\beta b_\alpha b_\beta [S_{\alpha\beta}(Q) - 1] \qquad (1)$$

is measured where α and β denote the chemical species, n is the number of different chemical species, c_α and b_α represent the atomic fraction and bound coherent scattering length of chemical species α, $\langle b\rangle = \sum_\alpha c_\alpha b_\alpha$ is the mean coherent scattering length, $S_{\alpha\beta}(Q)$ is a Faber-Ziman partial structure factor, and Q is the magnitude of the scattering vector [59]. The corresponding real-space information is represented by the total pair-distribution function $G_N(r)$ which is obtained from $S_N(Q)$ by using the Fourier transform relation

$$G_N(r) = 1 + \frac{1}{2\pi^2\rho r}\int_0^\infty [S_N(Q) - 1]\, M(Q)\sin(Qr) Q\, dQ, \qquad (2)$$

where ρ is the atomic number density of the glass and $M(Q)$ is a modification function defined by $M(Q) = 1$ for $Q \leqslant Q_{max}$, $M(Q) = 0$ for $Q > Q_{max}$. The latter is introduced because a diffractometer can measure only over a finite Q range up to a maximum value Q_{max}. However, if Q_{max} is sufficiently large that $S_N(Q)$ no longer shows structure at high Q, then $G_N(r)$ follows from Eq. (1) by replacing each $S_{\alpha\beta}(Q)$ by its corresponding partial pair-distribution function $g_{\alpha\beta}(r)$. To facilitate a comparison between the MD and experimental results, the reciprocal-space functions constructed from the simulations were Fourier transformed according to Eq. (2) with Q_{max} set at the experimental value. The severity of the Fourier transform artifacts associated with the first peak in $G_N(r)$ can be reduced by using a Lorch [60] modification function in Eq. (2), albeit at the expense of a broadening of this peak, where $M(Q) = \sin(aQ)/(aQ)$ for $Q \leqslant Q_{max}$, $a \equiv \pi/Q_{max}$, and $M(Q) = 0$ for $Q > Q_{max}$[61].

The x-ray total structure factor $S_X(Q)$ and total pair-distribution function $G_X(r)$ are given by Eqs. (1) and (2), respectively, after the coherent neutron scattering lengths b_α are replaced by the Q-dependent x-ray form factors with dispersion terms $f_\alpha(Q)$.

III. EXPERIMENT

The glassy samples were prepared from isotopically enriched boron (99.62% ^{11}B, 0.38% ^{10}B, Ceradyne Inc.) to minimize the effects of neutron absorbtion by ^{10}B. Approximately 5 g of B_2O_3 powder was first heated in a Pt-10%Rh crucible for 2 h at 200 °C to remove moisture. The sample was then melted in air at 1000 °C, held for 45 min, and poured into a P20 stainless tool steel mold to form a glass pellet. Excess glass was removed and the top of the pellet ground into the correct shape for the anvils of a Paris-Edinburgh (PE) press by using a rotary tool in a dry Ar filled glove bag. Indeed, the glass was always kept under dry conditions and the neutron diffraction experiments, which are highly sensitive to a small atomic fraction of light hydrogen, did not reveal any sample contamination. The density of the as-prepared isotopically enriched glass was measured to be 1.800(4) g cm^{-3} by using a helium pycnometer, giving a number density $\rho = 0.0774(2)$ Å^{-3} that is within 1% of the values reported elsewhere [21,39].

The high-pressure neutron diffraction experiments were made at ambient temperature ($T \sim 300$ K) using either the diffractometer D4c at the steady-state reactor source of the Institut Laue-Langevin [62] or the time-of-flight diffractometer PEARL at the ISIS pulsed neutron source. The samples were held in gaskets made from a $Ti_{0.676}Zr_{0.324}$ alloy which has a zero coherent neutron scattering length. The coherent neutron scattering lengths for boron and oxygen, taking into account the isotopic enrichment of the boron, are $b_{^{11}B} = 6.62(4)$ fm and $b_O = 5.803(4)$ fm [63].

As shown in Fig. 1, there are several sets of results for the pressure dependence of the density of B_2O_3 glass from both experiment and simulation [1,25,30,38,39]. In the present work, the diffraction data were analyzed using the results of Brazhkin *et al.* [39] which were obtained from *in situ* experiments using a strain gauge technique, where the sample (protected by a lacquer coating) and an ethanol-methanol or pentane-isopentane pressure transmitting medium were held within a toroid high-pressure cell. Several of the results from Ref. [25] are unreliable owing to sample contamination [27]. In the work of Huang *et al.* [38] elastic deformation was assumed when analyzing Brillouin scattering results and, since permanent densification occurs, the data provide a lower bound for the pressure-dependent density.

A. D4c diffraction experiments

The D4c experiment took advantage of a new focusing monochromator to increase the flux of neutrons at an incident wavelength of ∼0.5 Å, thereby extending Q_{max} from ≃15.45 Å^{-1} as used in previous work [53,54,56] to 21.7 Å^{-1}, which leads via Eq. (2) to an enhanced resolution of $G_N(r)$.

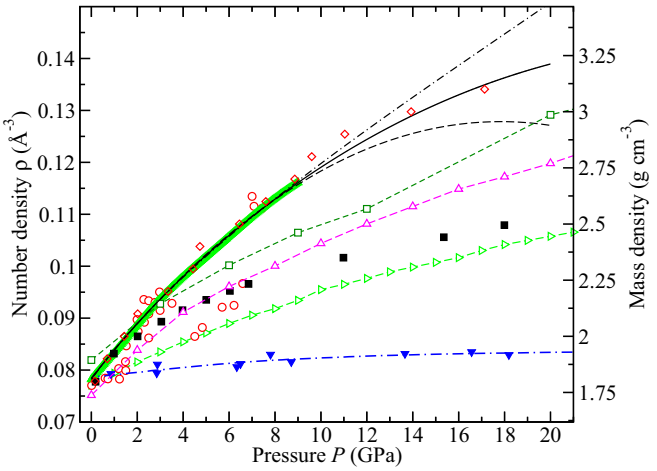

FIG. 1. (Color online) The density of B_2O_3 as measured for (i) cold compression of the glass in the *in situ* experiments by Brazhkin *et al.* [39] [thick, light (green) curve with ▲ symbols]; (ii) the glass recovered to ambient conditions after quenching the melt at high pressure in the experiments by Brazhkin *et al.* [25] [(red) ○]; (iii) cold compression of the glass in the *in situ* Brillouin scattering experiments by Huang *et al.* [38] [(black) ■]; and (iv) the glass recovered to ambient conditions after cold compression in the experiments by Bridgeman and Šimon [1] [(blue) ▼] where the chained (blue) curve gives the fit taken from Ref. [1]. The data of Brazhkin *et al.* [39] were used to fit both a third-order Birch-Murnaghan equation of state [chained (black) curve] and a second-order polynomial [broken (black) curve], and the average of these fits is given by the solid (black) curve. The experimental data sets are compared to the MD results for cold compression of the glass from Brazhkin *et al.* [39] [broken (green) curve with □ symbols], Takada [30] [broken (magenta) curve with △ symbols] and Huang *et al.* [38] for an initial model with $f = 0.63$ [broken (green) curve with ▷ symbols], and to the present AIM MD results for an initial model with $f = 0.75$ [(red) ◇].

The experiment employed a VX5/180-type PE press (piston area of 66.5 cm^2) with cubic BN anvils having a single-toroid profile [64], giving reliable access to pressures up to ∼8 GPa. The press was mounted so that the incident and scattered beams were in the same plane, perpendicular to the axis along which load is applied to the anvils. Upon increasing the applied load, the sample position changes with piston displacement. The PE press was therefore mounted on a platform that could be translated vertically (z-axis drive) in order to center the sample in the incident beam at each pressure point with the aid of an optical camera [56]. The background scattering was minimized by optimizing the setup given in Ref. [54]. The incident neutron wavelength of $\lambda = 0.4951(1)$ Å and zero scattering angle for the detectors were measured using Ni powder contained within an encapsulated $Ti_{0.676}Zr_{0.324}$ gasket [65] mounted in the PE press with no applied load. Higher-order ($\lambda/2$) scattering was suppressed by placing a Rh filter after the Cu(220) monochromator, upstream of the sample position.

Diffraction patterns were measured for (a) the sample in its Ti-Zr gasket at different pressures, (b) an un-squashed empty Ti-Zr gasket, (c) several empty Ti-Zr gaskets that had been recovered from different high pressures in order to estimate the gasket scattering under load, and (d) the empty anvils. To assist in the data normalization at different pressures, where the anvils have different separations, additional diffraction patterns were measured at ambient pressure for large and small vanadium pellets contained in unsquashed and recovered (i.e., previously squashed) Ti-Zr gaskets, respectively. The data analysis followed the procedure described elsewhere [54]. The sample pressure was deduced from the load applied to the anvils of the press by using a calibration curve that has been extensively checked [54,55]. The pressure dependence of the sample density was taken directly from the data of Brazhkin *et al.* [39] (Fig. 1).

At the end of the high-pressure experiment, the sample was decompressed from 8.2 GPa over 1 h and a diffraction pattern was taken of the recovered sample while it remained in the PE press. It was not possible to measure the density of the recovered sample because it shattered into a fine powder on removal from the press. The density of the relaxed glass as recovered to ambient from a pressure of 5.6 or 9 GPa is expected to be ∼6% greater than the uncompressed density [21,39]. It takes, however, many days for B_2O_3 glass to fully relax following pressure release [1,21]. The position of the first sharp diffraction peak (FSDP) Q_{FSDP} was therefore plotted against density ρ for the B_2O_3 sample on loading, and the density of the recovered sample was estimated from the position of its FSDP at 1.86(2) Å^{-1} to be $\rho = 0.0944$ Å^{-3}, which is ∼21% larger than the uncompressed density. In comparison, the compacted glass made by quenching the melt from 1200 °C to room temperature at 4 GPa is 22.5%–27% larger than the uncompressed density [7,45].

In a separate diffraction experiment at ambient pressure, a powdered glass sample was held in a vanadium container of inner diameter 4.8 mm and 0.1 mm wall thickness. The incident neutron wavelength was 0.4986(1) Å. Diffraction patterns were taken for the sample in its container, the empty container, the empty instrument, and a cylindrical vanadium rod of diameter 6.072(6) mm for normalization purposes. A diffraction pattern was also measured for a bar of neutron absorbing $^{10}B_4C$ of dimensions comparable to the sample to account for the effect of the sample attenuation on the background signal at small scattering angles. As for the high-pressure experiment, each complete diffraction pattern was built up from the intensities measured for different positions of D4c's group of nine microstrip detectors. These intensities were saved at regular intervals to check the sample and diffractometer stabilities. The data were analyzed by using a standard procedure [66].

B. PEARL diffraction experiment

The PEARL experiment employed a V3 variant PE press [67] (piston area of 102 cm^2) with sintered diamond anvils having a double-toroid profile that enables pressures in excess of 8 GPa to be reliably obtained [68]. The press was mounted using a transverse geometry such that the incident beam was directed along the compression axis through the anvil mounted on the breach of the press, and the scattered beam was observed by detectors mounted at a scattering angle $2\theta \simeq 90°$. Upon increasing the applied load, the sample position relative to the detectors changes with piston displacement. The press assembly for each pressure

point was therefore moved using a motorized system to ensure that the sample was correctly centered in the diffractometer. The background scattering was minimized by using the setup described in Ref. [55].

Diffraction patterns were measured for an empty Ti-Zr gasket with a small applied load and for the sample in its gasket at several different pressures. To normalize the data sets, diffraction patterns were also measured for a piece of vanadium contained in a Ti-Zr gasket at comparable loads to the sample in order to match the sample geometry at each pressure point. The measurement protocol and data analysis procedure, including the use of a Lorentzian function to extrapolate the measured $S_N(Q)$ functions to $Q = 0$ for use in Eq. (2), are described in detail elsewhere [55]. The sample pressure was determined from the load applied to the anvils by constructing a calibration curve based on the results obtained from several independent neutron diffraction experiments [55]. The sample density at pressures >9 GPa was estimated by fitting the data of Brazhkin *et al.* [39] using (i) a third-order Birch-Murnaghan equation of state [68] or (ii) a second-order polynomial. The Birch-Murnaghan fit gave an isothermal bulk modulus at ambient pressure of $B_0 = 12.70(3)$ GPa with a first pressure derivative at ambient pressure of $B_0' = 3.13(1)$ (Fig. 1) where the former compares to a value of $B_0 = 13.8$ GPa from Ref. [39] and to values for the adiabatic bulk modulus of 12.1 GPa (Ref. [69]), 13.2 GPa (Ref. [70]), or 11.67 GPa [46]. The diffraction data for pressures of 13.0(5) and 17.5(5) GPa were analyzed by using both sets of density values, and also by using the average of these density values (Fig. 1). In the following, and unless otherwise stated, the quoted results for the highest two pressures correspond to these averaged density values. Use in the data analysis of a different density value at a given pressure leads to a scaling of the $G_N(r)$ function such that the peak positions remain the same but there is a change to the B-O coordination number.

IV. MOLECULAR DYNAMICS SIMULATIONS

A. AIM for B_2O_3

MD simulations were performed using an AIM in which the *shape* of the anions is allowed to change in response to their coordination environment [71]. This is achieved by modifying the distance r^{ij} between two ions i and j to give a revised distance

$$\rho^{ij} = r^{ij} - \delta\sigma^i - \delta\sigma^j - \mathbb{S}^{(1)}_\alpha\left(\nu^i_\alpha - \nu^j_\alpha\right) - \mathbb{S}^{(2)}_{\alpha\beta}\left(\kappa^i_{\alpha\beta} + \kappa^j_{\alpha\beta}\right), \tag{3}$$

where the variables characterize the change in shape of the ions. $\delta\sigma^i$ is a scalar that represents the deviation of the radius of ion i from its default value, ν^i and κ^i are sets of three and five variables describing the dipolar and quadrupolar shape distortions, respectively, while $\mathbb{S}^{(1)}$ and $\mathbb{S}^{(2)}$ are the corresponding interaction tensors:

$$\mathbb{S}^{(1)}_\alpha = \frac{r^{ij}_\alpha}{r^{ij}}, \tag{4}$$

$$\mathbb{S}^{(2)}_{\alpha\beta} = \frac{3r^{ij}_\alpha r^{ij}_\beta}{{r^{ij}}^2} - \delta_{\alpha\beta}, \tag{5}$$

and $\delta_{\alpha\beta}$ is the Kronecker delta. The Einstein summation convention is used for tensor products. The total potential energy for the AIM is written as the sum $V^{\text{tot}} = V^{\text{rep}} + V^{\text{disp}} + V^{\text{Coul}} + V^{\text{pol}}$ where V^{rep} is the contribution from overlap repulsion, V^{disp} is the contribution from dispersion, V^{Coul} is the Coulomb contribution, and V^{pol} is the contribution from polarization.

As a consequence of Eq. (3), the repulsion term V^{rep} of the commonly used Born-Huggins-Mayer interaction potential takes the form

$$\begin{aligned} V^{\text{rep}} = &\sum_{i\in\text{B},\, j\in\text{O}} \left[A^{+-}\exp(-a^{+-}\rho^{ij}) + B^{+-}\exp(-b^{+-}\rho^{ij})\right] \\ &+ \sum_{i\in\text{O},\, j\in\text{O},\, i<j} A^{--}\exp(-a^{--}\rho^{ij}) \\ &+ \sum_{i\in\text{B},\, j\in\text{B},\, i<j} A^{++}\exp(-a^{++}r^{ij}) \\ &+ \sum_{i\in\text{O}} \{D[\exp(\beta\delta\sigma^i) + \exp(-\beta\delta\sigma^i)] \\ &+ [\exp(\zeta^2 \mid \nu^i \mid^2) - 1] + [\exp(\eta^2 \mid \kappa^i \mid^2) - 1]\}, \end{aligned} \tag{6}$$

where

$$|\kappa^i|^2 = {\kappa^i_{xx}}^2 + {\kappa^i_{yy}}^2 + {\kappa^i_{zz}}^2 + 2\left({\kappa^i_{xy}}^2 + {\kappa^i_{xz}}^2 + {\kappa^i_{yz}}^2\right). \tag{7}$$

Note that in the expression for V^{rep}, the cation-cation term uses r^{ij} because cations are not allowed to change shape. The last summations include the self-energy terms, which correspond to the cost in energy of deforming the anion charge density. The effective force constants β, ζ, and η set the difficulty for deformation of an anion in a spherical, dipolar, or quadrupolar fashion, respectively.

In the AIM, $\{\delta\sigma^N, \nu^N_x, \nu^N_y, \nu^N_z, \kappa^N_{xx}, \kappa^N_{yy}, \kappa^N_{zz}, \kappa^N_{xy}, \kappa^N_{xz}, \kappa^N_{yz}\}$ are treated as additional degrees of freedom, where N is the total number of ions in the system. The forces on the ions are calculated at each time step of the simulation by minimizing the total potential energy using a conjugate gradient method. The forces therefore depend on the positions of all the other ions in the simulation cell, which confers the AIM model with a many-body character even though the total energy is written as a sum of individual or pair components.

The dispersion term includes dipole-dipole and dipole-quadrupole terms

$$V^{\text{disp}} = -\sum_{i<j}\left[f^{ij}_6(r^{ij})\frac{C^{ij}_6}{(r^{ij})^6} + f^{ij}_8(r^{ij})\frac{C^{ij}_8}{(r^{ij})^8}\right], \tag{8}$$

where C^{ij}_6 (C^{ij}_8) is the dipole-dipole (dipole-quadrupole) dispersion coefficient, and $f^{ij}_n(r^{ij})$ ($n = 6$ or 8) are damping functions [72] that describe the short-range penetration correction to the asymptotic multipole expansion for the dispersion. They take the form

$$f^{ij}_n(r^{ij}) = 1 - e^{-b^{ij}_n r^{ij}}\sum_{k=0}^{n}\frac{\left(b^{ij}_n r^{ij}\right)^k}{k!}, \tag{9}$$

where the parameter b^{ij}_n is the inverse of the length at which the correction is first taken into account, and the limiting values are $f^{ij}_n(0) = 0$ and $f^{ij}_n(\infty) = 1$.

Finally, the electrostatic interactions are dealt with by treating the ions as polarizable [73,74]. In addition to the Coulomb term

$$V^{\mathrm{Coul}} = \sum_{i<j} \frac{q^i q^j}{r^{ij}}, \tag{10}$$

where formal charges q^i are used for both ions, we include a polarization term which takes the form

$$V^{\mathrm{pol}} = \sum_{i<j} \left[q^i \, \mu_\alpha^j \, g_D^{ij}(r^{ij}) - q^j \, \mu_\alpha^i \, g_D^{ji}(r^{ij}) \right] \mathbb{T}_\alpha^{(1)} - \sum_{i<j} \mu_\alpha^i \, \mu_\beta^j \, \mathbb{T}_{\alpha\beta}^{(2)} + \sum_i \frac{1}{2\alpha^i} \mid \mu^i \mid^2 , \tag{11}$$

where $\{\mu_x^N, \mu_y^N, \mu_z^N\}$ are additional degrees of freedom representing the induced ion dipoles. $\mathbb{T}_\alpha^{(1)}$ and $\mathbb{T}_{\alpha\beta}^{(2)}$ are the charge-dipole and dipole-dipole interaction tensors, and α^i is the polarizability of ion i. The polarizability of the boron ions is neglected, so the model contains only a single value α which describes the polarizability of the oxide ions. Again, we include short-range induction effects which are due to the high compression of ions in condensed ionic materials [75–77]. These effects are included straightforwardly through the use of damping functions similar to those used for the dispersion term:

$$g_D^{ij}(r^{ij}) = 1 - c_D^{ij} e^{-b_D^{ij} r^{ij}} \sum_{k=0}^{4} \frac{\left(b_D^{ij} r^{ij}\right)^k}{k!}. \tag{12}$$

Here c_D^{ij} is a parameter that reflects the amplitude of this damping at ion j due to the presence of ion i, and b_D^{ij} is again a short-range parameter. As for the other degrees of freedom, the induced dipoles were determined at each time step of the simulation by minimizing V^{pol} using a conjugate gradient method.

The sets of parameters used to describe V^{rep} and V^{pol}, which are summarized in Table I, were obtained by fitting the forces and dipoles obtained *ab initio* from a series of condensed-phase calculations. These calculations were carried out on the glassy configurations of B_2O_3 obtained in Ref. [37], which contain 100 atoms and with the fraction of B atoms in boroxol rings f varying from 0 to 0.22. The general procedure is described in detail in Refs. [58,78]. The parameters for the dispersion term were taken from Jahn *et al.* [79].

B. Simulation details

The initial configuration used for the present MD simulations was taken from the boroxol-rich model described in Ref. [37]: It contains $N = 320$ atoms (128 B and 192 O), a large number of boroxol rings ($f = 0.75$), and has a density that corresponds to the measured density of the glass under ambient conditions. This model was originally constructed by Takada *et al.* [30] and was later refined *ab initio* in Ref. [37]. A time step of 1 fs was used for all of the simulations, and the Coulomb and polarization forces were calculated using the Ewald summation method. Short runs of a few tens of picosecond duration were first made using the NPT ensemble for several target pressures, where P and T denote the pressure and temperature, respectively. Each run provided a cell size and starting configuration for a simulation in the NVT ensemble of at least 1 ns duration, where V denotes the volume. The modeled pressures indicated throughout the paper are the average values obtained from these (constant density) NVT runs. As seen in Fig. 1, the AIM MD simulations reproduce the pressure dependence of the density over the whole pressure range (0–10 GPa) probed in the *in situ* experiments of Brazhkin *et al.* [39]. The agreement possibly extends beyond this range since the simulated data fall in between various extrapolations of the experimental data [39]. As emphasized by Fig. 1, the ability of the AIM to reproduce the measured equation of state represents a marked improvement relative to previous models [30,38,39].

The partial pair-distribution functions and partial structure factors were extracted directly from the trajectories. The latter were computed using

$$S_{\alpha\beta}(Q) = \langle \hat{\rho}_\alpha(\mathbf{Q}) \hat{\rho}_\beta^*(\mathbf{Q}) \rangle, \tag{13}$$

where the dynamical variable $\hat{\rho}_\alpha(\mathbf{Q})$ represents the Fourier component of the atomic density of type α atoms at wave vector $\mathbf{Q}$:

$$\hat{\rho}_\alpha(\mathbf{Q}) = N_\alpha^{-1/2} \sum_{i=1}^{N_\alpha} \exp(i \mathbf{Q} \cdot \mathbf{r_i}), \tag{14}$$

$\mathbf{r_i}$ is the position of atom i, and N_α is the number of atoms of type α in the system. The angular brackets denote a thermal average, which was in practice evaluated as the time average over the duration of a simulation. For consistency with the experimental results, the total structure factors and total pair-distribution functions were deduced from the partial structure factors by using Eqs. (1) and (2).

TABLE I. Parameters used in the AIM for B_2O_3 where all values are in atomic units. Values for b_D^{++} and c_D^{++} are not given (the notation implies that ions labeled as i and j are both positive): Since the polarizability of the boron ions is neglected, the terms $\mu_\alpha^+ = 0$ in Eq. (11) such that $g_D^{++}(r^{++})$ does not need to be defined.

A^{++}	62.630	a^{++}	3.9720	A^{--}	2,227.6	a^{--}	2.6105
A^{+-}	15.798	a^{+-}	1.5465	B^{+-}	34,636	b^{+-}	4.8366
b_D^{+-}	2.1152	b_D^{--}	2.6858	c_D^{+-}	1.2479	c_D^{--}	2.5455
C_6^{--}	25.4	$C_6^{+-} = C_8^{+-}$	0.0	C_8^{--}	491.6	$C_6^{++} = C_8^{++}$	0.0
$b_6^{--} = b_8^{--}$	2.000	$b_6^{+-} = b_8^{+-}$	2.000	$b_6^{++} = b_8^{++}$	2.000	D	0.6981
β	1.8973	ζ	1.6230	η	7.4572	α	8.7893

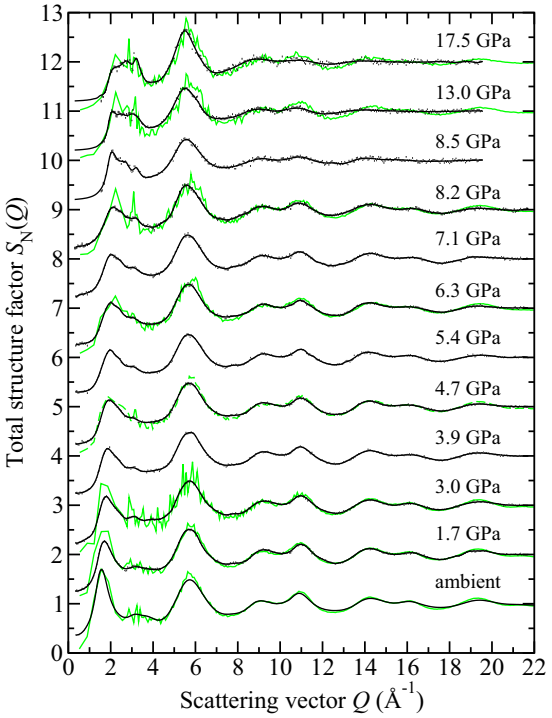

FIG. 2. (Color online) The pressure dependence of the neutron total structure factor $S_N(Q)$ for B_2O_3 glass as measured using the D4c [ambient pressure to 8.2(5) GPa] or PEARL [8.5(5)–17.5(5) GPa] diffractometer. Vertical bars give the statistical errors on the measured data points, and solid (black) curves give spline fits to the data sets. In the case of the PEARL experiments, the region $Q \leqslant 1.55$ Å^{-1} was not accessible and the solid (black) curves for this region correspond to fitted Lorentzian functions (see the text). The results are compared to those obtained from the AIM MD simulations at pressures of 0.16, 1.43, 3.34, 4.74, 6.45, 8.86, 13.93, and 17.46 GPa [light solid (green) curves]. The high-pressure data sets have been shifted vertically for clarity of presentation.

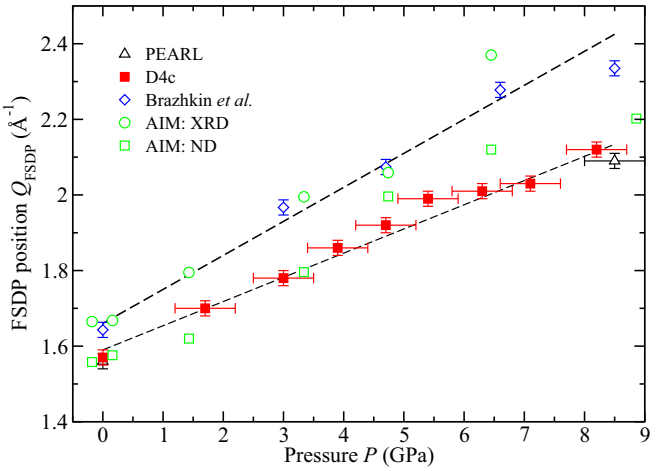

FIG. 3. (Color online) The pressure dependence of the FSDP position Q_{FSDP} as measured in the present neutron diffraction work using the D4c [(red) ■] or PEARL [(black) △] diffractometer. The results are compared to those obtained from the x-ray diffraction work of Brazhkin *et al.* [39] [(blue) ◇] and from the AIM MD simulations of $S_N(Q)$ [(green) □] and $S_X(Q)$ [(green) ○]. The broken curves give straight-line fits to the measured neutron or x-ray diffraction results.

V. RESULTS

The neutron total structure factors $S_N(Q)$ for B_2O_3 glass measured in the pressure range from ambient to 17.5 GPa are shown in Fig. 2 together with the AIM MD results. The neutron diffraction results show a reduction in height of the FSDP and an almost linear increase of its position Q_{FSDP} as the pressure is increased from ambient to ∼8.5 GPa (Fig. 3). At higher pressures it becomes difficult to discern the FSDP from the principal peak which appears as a small feature at $\simeq$3 Å^{-1} under ambient conditions [80]. These observations are reproduced by the MD simulations as shown in Figs. 2 and 3. The x-ray diffraction results of Brazhkin *et al.* [39] also show an almost linear increase of Q_{FSDP} with pressure, but there are differences in the position and gradient which may arise from the different weighting factors for the partial structure factors that contribute towards the FSDP in neutron versus x-ray diffraction experiments on B_2O_3 glass. This conjecture is supported by the fact that the MD results reproduce the trends shown by both neutron and x-ray diffraction (Fig. 3).

The pressure dependence of the measured and simulated $G_N(r)$ functions is shown in Fig. 4. The MD results account for all of the main features in the measured data sets although the

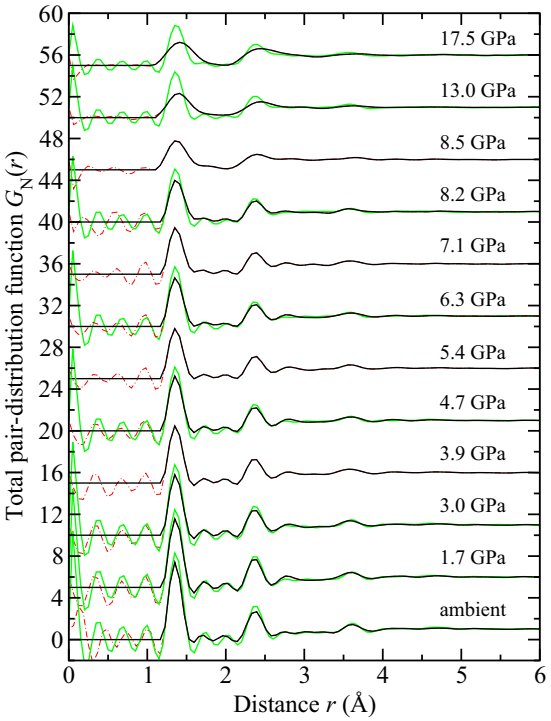

FIG. 4. (Color online) The solid (black) curves show the measured $G_N(r)$ functions obtained by Fourier transforming the $S_N(Q)$ functions given by the solid (black) curves in Fig. 2. The chained (red) curves show the Fourier transform artifacts at r values smaller than the distance of closest approach between two atoms, and oscillate about the calculated $G_N(r \to 0) = 0$ limiting values as shown by the solid (black) curves in the small-r region. The light solid (green) curves show the AIM $G_N(r)$ functions obtained by Fourier transforming the corresponding $S_N(Q)$ functions given in Fig. 2 following the same procedure used for the measured data sets.

TABLE II. Parameters describing the pressure dependence of the structure of B_2O_3 glass as measured using the D4c or PEARL diffractometer. The number density ρ of the glass is given (see Fig. 1) together with the B-O bond distance r_{BO} as taken from the position of the first peak in $G_N(r)$, the positions r_2, r_3, and r_4 of the second, third, and fourth peaks in $G_N(r)$, the ratio r_2/r_{BO}, and the mean B-O coordination number $\bar{n}_B^O$. The $\bar{n}_B^O$ values were obtained by integrating over the first peak in $G_N(r)$ to the first minimum where, in the case of the D4c data sets, the Fourier transform artifacts shown in Fig. 4 were reduced by using Eq. (2) with a Lorch [60] modification function. For the 13.0 and 17.5 GPa data sets, ρ corresponds to the mean of the extrapolated values obtained from third-order Birch-Murnaghan and second-order polynomial fits to the data of Brazhkin *et al.* [39] (Fig. 1).

Pressure (GPa)	Instrument	ρ (Å^{-3})	r_{BO} (Å)	r_2 (Å)	r_3 (Å)	r_4 (Å)	r_2/r_{BO}	$\bar{n}_B^O$
Ambient	D4c	0.0782(1)	1.35(1)	2.37(2)	2.75(3)	3.61(1)	1.754	3.0(1)
1.7(5)	D4c	0.0876(1)	1.36(1)	2.37(2)	2.78(3)	3.59(2)	1.742	2.9(1)
3.0(5)	D4c	0.0938(1)	1.36(1)	2.37(2)	2.79(3)	3.59(2)	1.743	2.9(1)
3.9(5)	D4c	0.0977(1)	1.36(1)	2.37(2)	2.79(3)	3.59(2)	1.742	2.9(1)
4.7(5)	D4c	0.1010(1)	1.36(1)	2.37(2)	2.79(3)	3.60(2)	1.748	2.9(1)
5.4(5)	D4c	0.1040(1)	1.36(1)	2.38(2)	2.80(3)	3.59(2)	1.752	3.0(1)
6.3(5)	D4c	0.1067(1)	1.36(1)	2.38(2)	2.78(3)	3.53(2)	1.749	3.0(1)
7.1(5)	D4c	0.1096(1)	1.36(1)	2.38(2)	2.77(3)	3.58(1)	1.749	3.3(1)
8.2(5)	D4c	0.1134(1)	1.37(1)	2.38(2)	2.76(3)	3.57(2)	1.740	3.4(1)
8.5(5)	PEARL	0.1145(1)	1.37(1)	2.40(2)	2.82(3)	3.66(2)	1.753	3.4(1)
13.0(5)	PEARL	0.1268(1)	1.40(1)	2.44(2)	2.81(3)	3.64(3)	1.747	3.7(1)
17.5(5)	PEARL	0.1355(1)	1.42(1)	2.45(2)	–	3.70(3)	1.726	3.8(1)
Recovered	D4c	0.0944(1)	1.35(1)	2.38(2)	2.83(3)	3.61(2)	1.758	3.0(1)

first peak in $G_N(r)$, which is associated with nearest-neighbor B-O correlations, is sharper than found by experiment at the highest pressures. Some of this discrepancy may result from experimental artifacts since features in the D4c data set at 8.2 GPa are broader than for the PEARL data set at 8.5 GPa. Several of the parameters describing the measured $G_N(r)$ functions are listed in Table II and, in the remainder of this section, the quoted r-space values are those obtained from neutron diffraction unless otherwise specified.

As the pressure is increased to 6.3 GPa, there is no change to the nearest-neighbor bond distance $r_{BO} = 1.35(2)$ Å or coordination number $\bar{n}_B^O \simeq 3$. At higher pressures, however, the first peak in $G_N(r)$ is broadened on its high-r side and eventually shifts position to higher r values as the B-O coordination number increases. For example, the first peak in $G_N(r)$ is at the same position for both 6.3 and 7.1 GPa, but there is a high-r shoulder at the higher pressure which leads to $\bar{n}_B^O > 3$. At the highest pressure of 17.5 GPa, the first peak position is shifted to 1.42(2) Å and the asymmetrically broadened peak gives $\bar{n}_B^O = 3.8(1)$. In comparison, the high-pressure crystalline phase of B_2O_3 forms a network of distorted corner-sharing BO_4 tetrahedra in which there are three long bonds at an average distance $r_{BO} = 1.508$ Å and one short bond at $r_{BO} = 1.373$ Å [50].

As discussed in Sec. III B, there is some ambiguity in the number density for the highest pressure points of 13.0 and 17.5 GPa (Fig. 1). A reanalysis of the neutron diffraction data using density values taken from the Birch-Murnaghan equation of state fit led to $\bar{n}_B^O$ values of 3.8(1) and 4.1(1), respectively, while a reanalysis using the density values taken from the polynomial fit led to $\bar{n}_B^O$ values of 3.6(1) and 3.6(1), respectively. Since the polynomial fit shows a small reduction of the density when the pressure increases beyond 18 GPa (Fig. 1), it is likely to underestimate the high-pressure density of B_2O_3 glass leading to an underestimate of $\bar{n}_B^O$ at 17.5 GPa.

At ambient conditions, the second peak in $G_N(r)$ at $r_2 = 2.37(2)$ Å can be attributed to the O-O distances within BO_3 motifs and to the B-B distances between these motifs. These assignments are supported by the MD partial pair-distribution functions that are shown in Fig. 5. In the case of planar boroxol rings formed from regular equilateral BO_3 triangles (Fig. 6), these distances are equal such that $r_{OO}/r_{BO} = r_{BB}/r_{BO} = \sqrt{3} = 1.732$ [11]. From experiment, the measured ratio at ambient conditions $r_2/r_{BO} \sim 1.75$ (Table II) and changes little over the measured pressure range. In comparison, the mean distance ratios are $r_{OO}/r_{BO} = 1.63$ and $r_{BB}/r_{BO} = 1.78$ for the high-pressure crystalline phase of B_2O_3 [50]. At ambient conditions, the third and fourth peaks in $G_N(r)$ at $r_3 = 2.75(3)$ Å and $r_4 = 3.61(1)$ Å will have contributions from boron to second-neighbor oxygen distances. In the case of boroxol ring formation, $r_3/r_{BO} = 2$ if both atoms lie within a ring, and $r_4/r_{BO} = \sqrt{7}$ if the B atom within a ring has its second-neighbor oxygen atom outside of that ring (Fig. 6) [11]. The third peak is an observable feature in $G_N(r)$ at pressures up to ~13 GPa, while the fourth peak persists to pressures up to 17.5 GPa. If the third peak has a large contribution from boroxol rings, then its absence for pressures in excess of 13 GPa is consistent with the Raman scattering experiments of Grimsditch *et al.* [15] which show that the intensity of the boroxol ring breathing mode at 808 cm^{-1} vanishes at a pressure ~14 GPa.

The above interpretation is supported by the AIM MD simulations as shown in Figs. 7 and 8. Figure 7(a) shows the B-O partial pair-distribution functions in the range 2.5–3.25 Å as obtained from simulations of boroxol-poor and boroxol-rich models, where these simulations used initial configurations taken from Ref. [37]. The boroxol-rich model gives a distinct peak at $r_3 \simeq 2.75$ Å, which for the boroxol-poor model is shifted to higher r values and is broadened. As shown in Fig. 7(b), this shift of peak position is also observed on

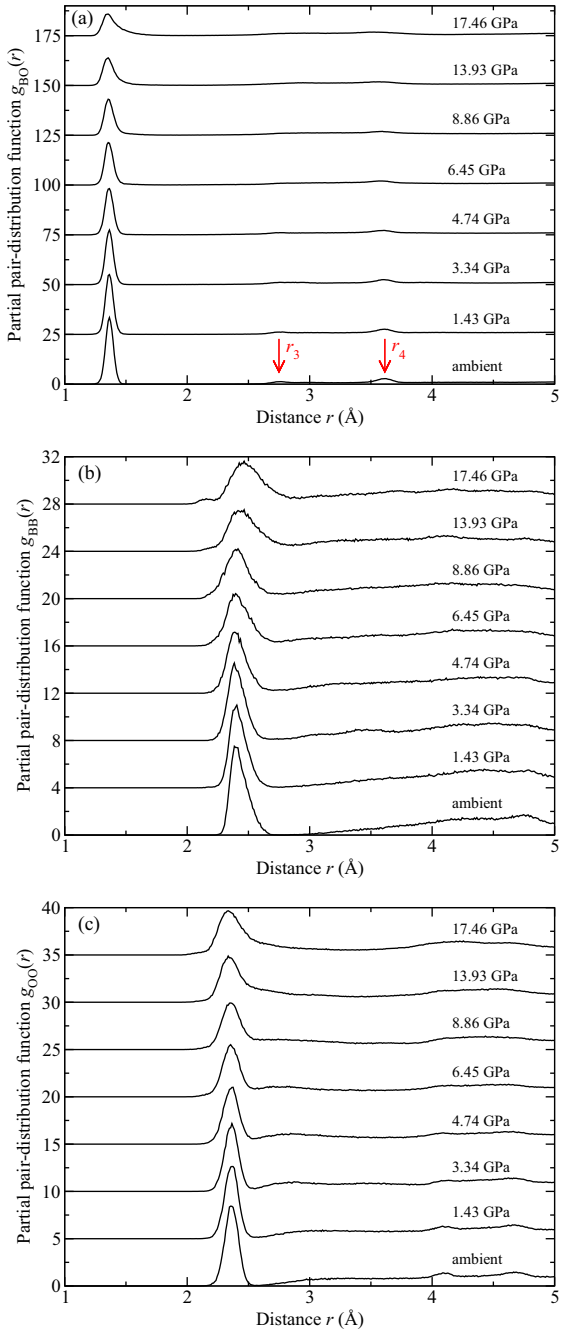

FIG. 5. (Color online) The pressure dependence of the partial pair-distribution functions for B_2O_3 glass as obtained from the AIM MD simulations: (a) $g_{BO}(r)$, (b) $g_{BB}(r)$, and (c) $g_{OO}(r)$. In (a) the vertical arrows point to small peaks in $g_{BO}(r)$ at $r_3 \simeq 2.75$ Å and $r_4 \simeq 3.61$ Å for the ambient pressure data set (see the text).

compression of the boroxol-rich glass model, and is consistent with a progressive dissolution of boroxol rings as shown in Fig. 8. Thus, experiment and simulation both provide a broadly self-consistent picture, although the dissolution mechanism is probably exaggerated in the simulations since the peak at $r_3 \simeq 2.75$ Å disappears at a lower pressure than found in experiment.

In Fig. 9(a), the $S_N(Q)$ function measured for the $^{11}B_2O_3$ sample recovered from a pressure of 8.2 GPa is compared to

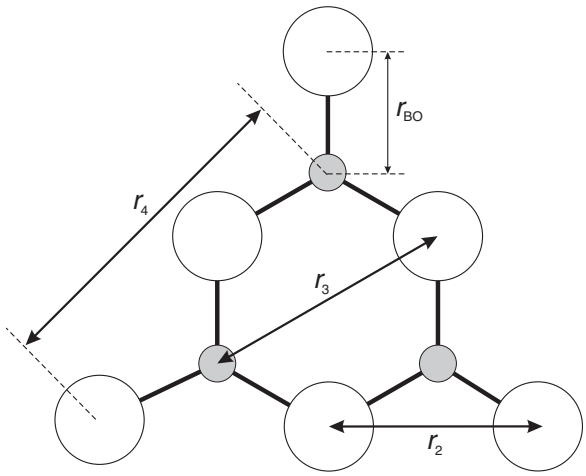

FIG. 6. Schematic of a planar B_3O_6 boroxol group showing several of the characteristic interatomic distances. The B and O atoms are indicated by the small shaded and large open circles, respectively.

the $S_N(Q)$ function measured for the uncompressed sample. The corresponding $G_N(r)$ functions are shown in Fig. 9(b) and several of the parameters describing these functions are listed in Table II. The r_{BO} values for the recovered and uncompressed samples are the same, but the FSDP for the recovered sample is reduced in height and is shifted to a higher Q value, which indicate a change to the intermediate range order. Use in the data analysis of recovered sample densities that are 6% and 21% greater than the uncompressed sample density (Sec. III A) led to $\bar{n}_B^O$ values of 2.8(1) and 3.0(1), respectively. This suggests that the higher density is more accurate, i.e., on decompression the glass was given sufficient time for BO_3 units to reform but insufficient time for the structure to fully relax.

For comparison with experiment, the AIM MD configuration obtained for 8.86 GPa (corresponding to a mass

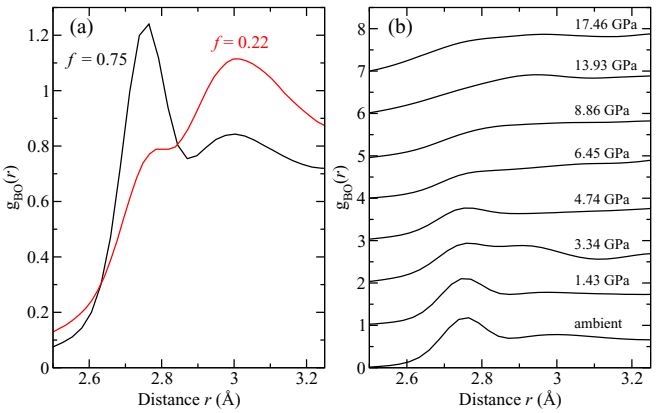

FIG. 7. (Color online) Zoom-in of the B-O partial pair-distribution function for an r range in which there is a signature of boroxol rings (see the text). (a) shows a comparison between the $g_{BO}(r)$ functions obtained from AIM MD simulations of boroxol-poor ($f = 0.22$) and boroxol-rich ($f = 0.75$) models at ambient density, and (b) shows the pressure dependence of $g_{BO}(r)$ from AIM MD simulations of the boroxol-rich model.

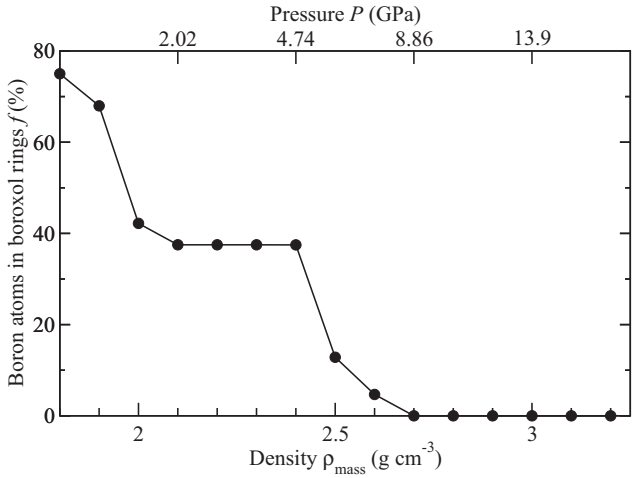

FIG. 8. The pressure (or density) dependence of the fraction f of boron atoms within boroxol rings as obtained from the AIM MD simulations of a boroxol-rich ($f = 0.75$) model at ambient pressure.

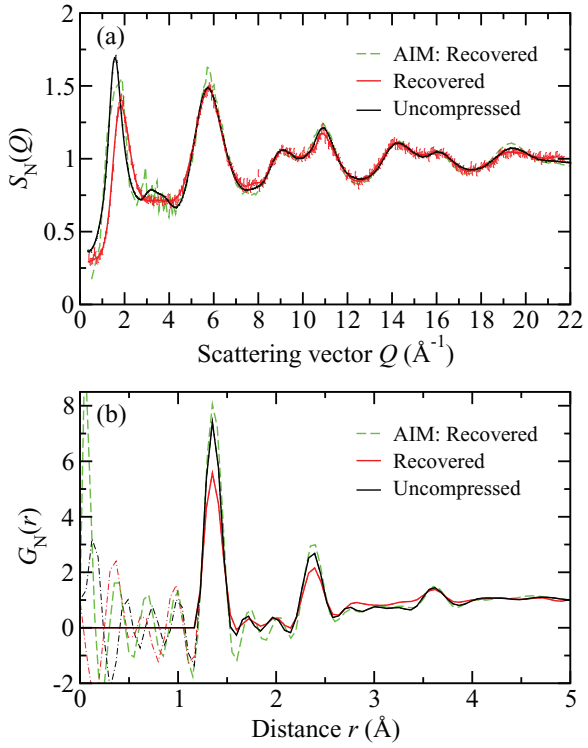

FIG. 9. (Color online) (a) The total neutron structure factor $S_N(Q)$ and (b) total neutron pair-distribution function $G_N(r)$ for B_2O_3 glass as measured before compression [solid (black) curves] or on recovery to ambient from a pressure of 8.2 GPa [light solid (red) curves]. The recovered data were analyzed using $\rho = 0.0944$ Å^{-3} (see the text). In (a) the vertical bars give the statistical errors on the measured data points, and the solid curves give spline fits. In (b) the $G_N(r)$ functions were obtained by Fourier transforming the spline fitted $S_N(Q)$ functions given in (a). The chained curves show the Fourier transform artifacts at r values smaller than the distance of closest approach between two atoms, and oscillate about the calculated $G_N(r \to 0) = 0$ limiting values as shown by the solid curves in the small-r region. The broken (green) curves in (a) and (b) show the AIM MD results for the glass recovered to ambient conditions from a pressure of 8.86 GPa.

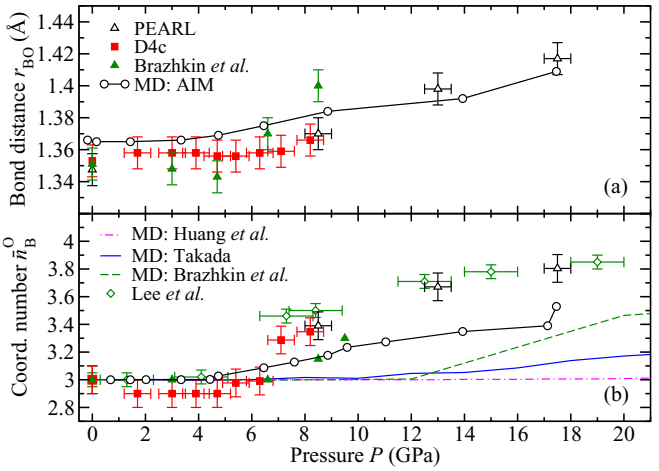

FIG. 10. (Color online) The pressure dependence at room temperature of the B-O (a) bond distance r_{BO} and (b) coordination number $\bar{n}_B^O$ as measured in (i) the present neutron diffraction work by using the D4c [(red) ■] or PEARL [(black) △] diffractometer, (ii) the x-ray diffraction work of Brazhkin *et al.* [39] [(green) ▲], or (iii) the x-ray inelastic scattering work of Lee *et al.* [31] [(green) ◇]. In (a) r_{BO} is taken from the position of the first peak in the measured total pair-distribution functions, and the results are compared to those obtained for the weighted mean position $\langle r_{BO} \rangle = \int dr\, r\, g_{BO}(r) / \int dr\, g_{BO}(r)$ from the AIM MD simulations [(black) ○]. In (b) the measured $\bar{n}_B^O$ values are compared to those found from the AIM MD simulations [(black) ○], the first-principles MD simulations of Brazhkin *et al.* [39] [broken (green) curve], and the empirical potential MD simulations of both Takada [30] [solid (blue) curve] and Huang *et al.* [38] [chained (magenta) curve].

density $\rho_{mass} = 2.7$ g cm^{-3}) was decompressed to ambient pressure ($\rho_{mass} = 1.84$ g cm^{-3}) via nine successive steps. In each step, the density was decreased by $\rho_{mass} \simeq 0.1$ g cm^{-3} within the NPT ensemble to provide a new cell size and starting configuration for an NVT simulation of 1 ns duration. In contrast to experiment, the simulations show much less difference between the uncompressed and recovered samples. In the decompression process, the MD simulations show a recovery of boroxol rings from $f = 0$ at 8.86 GPa to $f = 0.42$ at ambient pressure.

VI. DISCUSSION

As shown in Fig. 10, the neutron diffraction results for B_2O_3 glass under cold compression give a pressure dependence for r_{BO} and $\bar{n}_B^O$ that is in good overall accord with the x-ray diffraction results of Brazhkin *et al.* [39] and the inelastic x-ray scattering results of Lee *et al.* [31]. They show that there is no significant change to $\bar{n}_B^O$ until a pressure of 6.3 GPa is attained, but there is a steady increase at higher pressures to $\bar{n}_B^O = 3.8(1)$ at 17.5 GPa. This increase, which is consistent with a transformation from triangular BO_3 to tetrahedral BO_4 units, initially manifests itself by the appearance of a high-r shoulder on the first peak in $G_N(r)$. The role played by oxygen packing in the structural transformations of the network-forming motifs in B_2O_3 and other oxide glasses is discussed elsewhere [82].

The large changes with increasing pressure to the FSDP in both the neutron and x-ray diffraction patterns (Fig. 3) indicate a reorganization of the intermediate range order. Raman spectroscopy experiments show that as the pressure is increased to ∼11 GPa there is a sudden drop in the measured intensity of the boroxol ring breathing mode at 808 cm^{-1}, but there is some disagreement as to whether the mode is completely eliminated at this pressure or at a higher pressure of ∼14 GPa [15,28]. Notwithstanding, the observed changes to the intermediate range order are associated with a progressive decomposition of boroxol rings.

The first-principles MD simulations of Brazhkin *et al.* [39] and the empirical potential MD simulations of Takada [30] and Huang *et al.* [38] reproduce the measured $\bar{n}_B^O$ values in the pressure regime below ∼6 GPa but fail at higher pressures (Fig. 10). They also underestimate the pressure dependence of the glass density as shown in Fig. 1. In comparison, the AIM MD simulations show much better agreement with the measured $\bar{n}_B^O$ values and reproduce the measured equation of state. The AIM also gives a good account of the total structure factors and pair-distribution functions as measured by neutron diffraction in the present work (Figs. 2 and 4) and by x-ray diffraction in the work of Brazhkin *et al.* [39] (Figs. 11 and 12). This situation, where AIM MD simulations based on a classical force field lead to better agreement with experiment as compared to first-principles MD simulations [39], is to some extent unexpected. It could result either from a fortuitous cancellation of errors in our AIM simulations or from the shorter simulation time scale used in first-principles work [39]. However, even for the AIM simulations there is a tendency at pressures above 10 GPa to underestimate $\bar{n}_B^O$ and therefore the amount of BO_4 units. This could be due to an intrinsic defect of the AIM model (progressive lack of transferability at the highest pressures) and/or the allowance for an insufficient time (1 ns) for the simulated system to relax (this is anticipated given the time scale of typically several days reported experimentally [1,21].) A more complete analysis of the strengths and limitations of the AIM will be reported elsewhere.

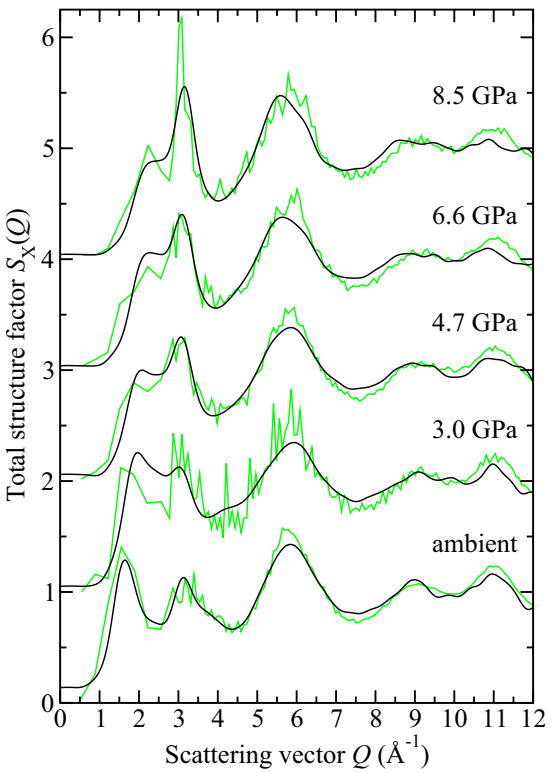

FIG. 11. (Color online) The pressure dependence of the x-ray total structure factor $S_X(Q)$ for B_2O_3 glass as measured by Brazhkin *et al.* [solid (black) curves] [39]. The results are compared to those obtained from the AIM MD simulations at pressures of 0.16, 3.34, 4.74, 6.45, and 8.86 GPa [light solid (green) curves)]. The high-pressure data sets have been shifted vertically for clarity of presentation.

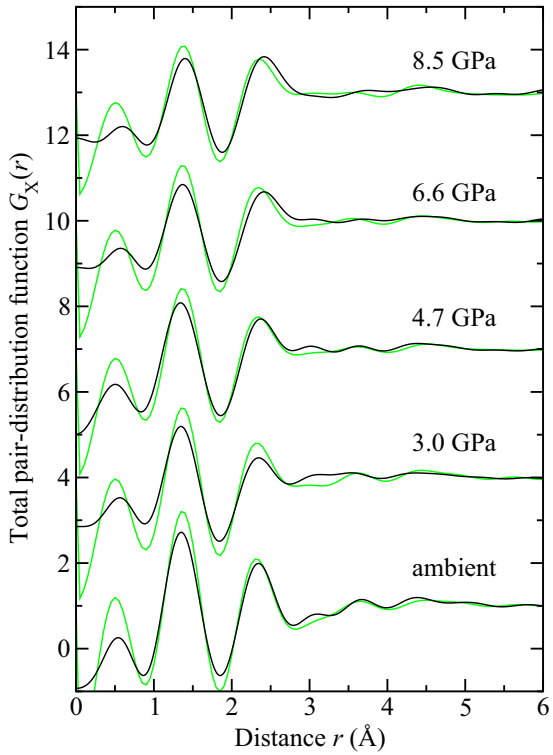

FIG. 12. (Color online) The pressure dependence of the measured x-ray total pair-distribution function $G_X(r)$ for B_2O_3 glass [solid (black) curves] as obtained by Fourier transforming the corresponding $S_X(Q)$ functions given in Fig. 11. The results are compared to those obtained by Fourier transforming the AIM MD $S_X(Q)$ functions shown in Fig. 11 using the same cutoff $Q_{max} = 10$ Å^{-1} as for the measured data sets [light solid (green) curves].

VII. CONCLUSIONS

The method of *in situ* high-pressure diffraction has been applied to B_2O_3 glass. The results tie together those obtained from previous x-ray diffraction [39], inelastic x-ray scattering [31], and Raman spectroscopy experiments [15,28] and show a three-stage densification process for B_2O_3 glass. First, as the pressure is increased from ambient to 6.3 GPa, triangular BO_3 motifs are retained but reorganize on an intermediate length scale as indicated by changes to the FSDP in both the neutron and x-ray diffraction patterns. For this

pressure range, the Raman spectroscopy experiments show a progressive dissolution of boroxol rings. As the pressure increases above 6.3 GPa, fourfold coordinated B atoms begin to appear in appreciable amounts and the dissolution of boroxol rings continues until a pressure of 11–14 GPa is attained. At larger pressures, the remaining BO_3 motifs are replaced by BO_4 motifs, a process that is not completed until the pressure exceeds 22.5 GPa [31]. These mechanisms are fully supported by the present AIM MD simulations.

Previous MD simulations do not reproduce the measured equation of state, nor the measured change in the B-O coordination number with increasing density [30,38,39]. In contrast, the newly designed AIM provides significantly improved results not only for the pressure dependance of the density but also for the structure as quantified by the total structure factors, total pair-distribution functions, and B-O coordination numbers. This agreement reinforces the importance of polarization effects in B_2O_3, and shows that the newly developed AIM is the model of choice for the investigation of B_2O_3 and borate glasses from low to moderately high pressures.

ACKNOWLEDGMENTS

It is a pleasure to thank Alain Bertoni, Jean-Luc Laborier, and Claude Payre for help with the D4c experiment and Chris Barry for help with the PEARL experiment. We would also like to acknowledge the EPSRC for support to the Bath group via Grants No. EP/G008795/1 and No. EP/J009741/1. K.W. thanks the EPSRC and D.A.J.W. thanks both the EPSRC and STFC for their Ph.D. studentships. We would also like to thank Vadim Brazhkin and Alexander Lyapin for helpful advice on the density of B_2O_3 glass under pressure and for providing numerical data sets from Ref. [39], Sung Keun Lee for providing numerical data sets from Ref. [31], and Keiron Pizzey for helping to assemble the data shown in Fig. 1. This work was supported by French state funds managed by the ANR within the Investissements d'Avenir programme under reference ANR-11-IDEX-0004-02, and more specifically within the framework of the Cluster of Excellence MATISSE. This work was performed using HPC resources from GENCI-CINES/IDRIS (Grant No. x2014081875).

[1] P. W. Bridgman and I. Šimon, J. Appl. Phys. **24**, 405 (1953).
[2] A. H. Silver and P. J. Bray, J. Chem. Phys. **29**, 984 (1958).
[3] J. Krogh-Moe, J. Non-Cryst. Solids **1**, 269 (1969).
[4] R. L. Mozzi and B. E. Warren, J. Appl. Crystallogr. **3**, 251 (1970).
[5] G. E. Jellison, Jr., L. W. Panek, P. J. Bray, and G. B. Rouse, Jr., J. Chem. Phys. **66**, 802 (1977).
[6] S. R. Elliott, Philos. Mag. B **37**, 435 (1978).
[7] S. K. Sharma, B. Simons, and J. F. Mammone, J. Non-Cryst. Solids **42**, 607 (1980).
[8] F. L. Galeener, G. Lucovsky, and J. C. Mikkelsen, Jr., Phys. Rev. B **22**, 3983 (1980).
[9] P. A. V. Johnson, A. C. Wright, and R. N. Sinclair, J. Non-Cryst. Solids **50**, 281 (1982).
[10] E. Chason and F. Spaepen, J. Appl. Phys. **64**, 4435 (1988).
[11] A. C. Hannon, D. I. Grimley, R. A. Hulme, A. C. Wright, and R. N. Sinclair, J. Non-Cryst. Solids **177**, 299 (1994).
[12] D. M. dos Santos-Loff, M. Micoulaut, and R. Kerner, Europhys. Lett. **28**, 573 (1994).
[13] R. E. Youngman and J. W. Zwanziger, J. Non-Cryst. Solids **168**, 293 (1994).
[14] R. E. Youngman, S. T. Haubrich, J. W. Zwanziger, M. T. Janicke, and B. F. Chmelka, Science **269**, 1416 (1995).
[15] M. Grimsditch, A. Polian, and A. C. Wright, Phys. Rev. B **54**, 152 (1996).
[16] R. Fernández-Perea, F. J. Bermejo, and M. L. Senent, Phys. Rev. B **54**, 6039 (1996).
[17] R. A. Barrio, R. Kerner, M. Micoulaut, and G. G. Naumis, J. Phys.: Condens. Matter **9**, 9219 (1997).
[18] S.-J. Hwang, C. Fernandez, J. P. Amoureux, J. Cho, S. W. Martin, and M. Pruski, Solid State Nucl. Magn. Reson. **8**, 109 (1997).
[19] J. Swenson and L. Börjesson, Phys. Rev. B **55**, 11138 (1997).
[20] R. N. Sinclair, C. E. Stone, A. C. Wright, I. G. Polyakova, N. M. Vedishcheva, B. A. Shakhmatkin, S. A. Feller, B. C. Johanson, P. Venhuizen, R. B. Williams, and A. C. Hannon, Phys. Chem. Glasses **41**, 286 (2000).
[21] A. C. Wright, C. E. Stone, R. N. Sinclair, N. Umesaki, N. Kitamura, K. Ura, N. Ohtori, and A. C. Hannon, Phys. Chem. Glasses **41**, 296 (2000).
[22] C. Joo, U. Werner-Zwanziger, and J. W. Zwanziger, J. Non-Cryst. Solids **261**, 282 (2000); **271**, 265 (2000).
[23] K. Suzuya, Y. Yoneda, S. Kohara, and N. Umesaki, Phys. Chem. Glasses **41**, 282 (2000).
[24] J. Diefenbacher and P. F. McMillan, J. Phys. Chem. A **105**, 7973 (2001).
[25] V. V. Brazhkin, Y. Katayama, Y. Inamura, M. V. Kondrin, A. G. Lyapin, S. V. Popova, and R. N. Voloshin, JETP Lett. **78**, 393 (2003).
[26] J. D. Nicholas, R. E. Youngman, S. V. Sinogeikin, J. D. Bass, and J. Kieffer, Phys. Chem. Glasses **44**, 249 (2003).
[27] V. V. Brazhkin, Y. Katayama, Y. Inamura, M. V. Kondrin, A. G. Lyapin, S. V. Popova, and R. N. Voloshin, JETP Lett. **79**, 308 (2004).
[28] J. Nicholas, S. Sinogeikin, J. Kieffer, and J. Bass, Phys. Rev. Lett. **92**, 215701 (2004).
[29] J. Nicholas, S. Sinogeikin, J. Kieffer, and J. Bass, J. Non-Cryst. Solids **349**, 30 (2004).
[30] A. Takada, Phys. Chem. Glasses **45**, 156 (2004).
[31] S. K. Lee, P. J. Eng, H.-K. Mao, Y. Meng, M. Newville, M. Y. Hu, and J. Shu, Nat. Mater. **4**, 851 (2005).
[32] S. K. Lee, K. Mibe, Y. Fei, G. D. Cody, and B. O. Mysen, Phys. Rev. Lett. **94**, 165507 (2005).
[33] P. Umari and A. Pasquarello, Phys. Rev. Lett. **95**, 137401 (2005).
[34] L. Huang and J. Kieffer, Phys. Rev. B **74**, 224107 (2006).
[35] J. Swenson and L. Börjesson, Phys. Rev. Lett. **96**, 199701 (2006).
[36] P. Umari and A. Pasquarello, Phys. Rev. Lett. **96**, 199702 (2006).

[37] G. Ferlat, T. Charpentier, A. P. Seitsonen, A. Takada, M. Lazzeri, L. Cormier, G. Calas, and F. Mauri, Phys. Rev. Lett. **101**, 065504 (2008).

[38] L. Huang, J. Nicholas, J. Kieffer, and J. Bass, J. Phys.: Condens. Matter **20**, 075107 (2008).

[39] V. V. Brazhkin, Y. Katayama, K. Trachenko, O. B. Tsiok, A. G. Lyapin, E. Artacho, M. Dove, G. Ferlat, Y. Inamura, and H. Saitoh, Phys. Rev. Lett. **101**, 035702 (2008).

[40] K. Trachenko, V. V. Brazhkin, G. Ferlat, M. T. Dove, and E. Artacho, Phys. Rev. B **78**, 172102 (2008).

[41] I. Hung, A. P. Howes, B. G. Parkinson, T. Anupõld, A. Samoson, S. P. Brown, P. F. Harrison, D. Holland, and R. J. Dupree, Solid State Chem. **182**, 2402 (2009).

[42] V. V. Brazhkin, O. B. Tsiok, and Y. Katayama, JETP Lett. **89**, 244 (2009).

[43] V. V. Brazhkin, I. Farnan, K.-I. Funakoshi, M. Kanzaki, Y. Katayama, A. G. Lyapin, and H. Saitoh, Phys. Rev. Lett. **105**, 115701 (2010).

[44] S. Ohmura and F. Shimojo, Phys. Rev. B **81**, 014208 (2010).

[45] G. Carini, Jr., E. Gilioli, G. Tripodo, and C. Vasi, Phys. Rev. B **84**, 024207 (2011).

[46] G. Carini, Jr., G. Carini, G. Tripodo, G. Di Marco, and E. Gilioli, Phys. Rev. B **85**, 094201 (2012).

[47] A. K. Soper, J. Phys.: Condens. Matter **23**, 365402 (2011).

[48] G. Ferlat, A. P. Seitsonen, M. Lazzeri, and F. Mauri, Nat. Mater. **11**, 925 (2012).

[49] G. E. Gurr, P. W. Montgomery, C. D. Knutson, and B. T. Gorres, Acta Crystallogr. B **26**, 906 (1970).

[50] C. T. Prewitt and R. D. Shannon, Acta Crystallogr. B **24**, 869 (1968).

[51] D. R. Uhlmann, J. F. Hays, and D. Turnbull, Phys. Chem. Glasses **8**, 1 (1967).

[52] M. J. Aziz, E. Nygren, J. F. Hays, and D. Turnbull, J. Appl. Phys. **57**, 2233 (1985).

[53] A. Zeidler, J. W. E. Drewitt, P. S. Salmon, A. C. Barnes, W. A. Crichton, S. Klotz, H. E. Fischer, C. J. Benmore, S. Ramos, and A. C. Hannon, J. Phys.: Condens. Matter **21**, 474217 (2009).

[54] J. W. E. Drewitt, P. S. Salmon, A. C. Barnes, S. Klotz, H. E. Fischer, and W. A. Crichton, Phys. Rev. B **81**, 014202 (2010).

[55] P. S. Salmon, J. W. E. Drewitt, D. A. J. Whittaker, A. Zeidler, K. Wezka, C. L. Bull, M. G. Tucker, M. C. Wilding, M. Guthrie, and D. Marrocchelli, J. Phys.: Condens. Matter **24**, 415102 (2012); **24**, 439601 (2012).

[56] K. Wezka, P. S. Salmon, A. Zeidler, D. A. J. Whittaker, J. W. E. Drewitt, S. Klotz, H. E. Fischer, and D. Marrocchelli, J. Phys.: Condens. Matter **24**, 502101 (2012).

[57] P. A. Madden and M. Wilson, Chem. Soc. Rev. **25**, 339 (1996).

[58] M. Salanne, B. Rotenberg, S. Jahn, R. Vuilleumier, C. Simon, and P. A. Madden, Theor. Chem. Acc. **131**, 1143 (2012).

[59] H. E. Fischer, A. C. Barnes, and P. S. Salmon, Rep. Prog. Phys. **69**, 233 (2006).

[60] E. Lorch, J. Phys. C: Solid State Phys. **2**, 229 (1969).

[61] P. S. Salmon, J. Phys.: Condens. Matter **18**, 11443 (2006).

[62] H. E. Fischer, G. J. Cuello, P. Palleau, D. Feltin, A. C. Barnes, Y. S. Badyal, and J. M. Simonson, Appl. Phys. A **74**, S160 (2002).

[63] V. F. Sears, Neutron News **3**, 26 (1992).

[64] S. Klotz, Th. Strässle, G. Rousse, G. Hamel, and V. Pomjakushin, Appl. Phys. Lett. **86**, 031917 (2005).

[65] W. G. Marshall and D. J. Francis, J. Appl. Crystallogr. **35**, 122 (2002).

[66] P. S. Salmon, S. Xin, and H. E. Fischer, Phys. Rev. B **58**, 6115 (1998).

[67] J. M. Besson, R. J. Nelmes, G. Hamel, J. S. Loveday, G. Weill, and S. Hull, Physica B **180-181**, 907 (1992).

[68] S. Klotz, *Techniques in High Pressure Neutron Scattering* (CRC Press, Boca Raton, FL, 2013).

[69] R. R. Shaw and D. R. Uhlmann, J. Non-Cryst. Solids **5**, 237 (1971).

[70] B. Bridge, N. D. Patel, and D. N. Waters, Phys. Status Solidi A **77**, 655 (1983).

[71] A. J. Rowley, P. Jemmer, M. Wilson, and P. A. Madden, J. Chem. Phys. **108**, 10209 (1998).

[72] K. T. Tang and J. P. Toennies, J. Chem. Phys. **80**, 3726 (1984).

[73] D. Marrocchelli, M. Salanne, P. A. Madden, C. Simon, and P. Turq, Mol. Phys. **107**, 443 (2009).

[74] D. Marrocchelli, M. Salanne, and P. A. Madden, J. Phys.: Condens. Matter **22**, 152102 (2010).

[75] P. W. Fowler and P. A. Madden, Phys. Rev. B **31**, 5443 (1985).

[76] C. Domene, P. W. Fowler, M. Wilson, and P. A. Madden, Mol. Phys. **100**, 3847 (2002).

[77] P. Jemmer, M. Wilson, P. A. Madden, and P. W. Fowler, J. Chem. Phys. **111**, 2038 (1999).

[78] A. Aguado, L. Bernasconi, S. Jahn, and P. A. Madden, Faraday Discuss. **124**, 171 (2003).

[79] S. Jahn and P. A. Madden, Phys. Earth Planet. Inter. **162**, 129 (2007).

[80] A principal peak or trough at $Q_{\mathrm{PP}} \simeq 2$–3 Å^{-1} appears in the partial structure factors for many glassy and liquid materials. For B_2O_3 glass, it manifests itself as a small peak in $S_{\mathrm{N}}(Q)$ because of a cancellation of the principal peaks in both $S_{\mathrm{BB}}(Q)$ and $S_{\mathrm{OO}}(Q)$ with a principal trough in $S_{\mathrm{BO}}(Q)$. An analogous situation occurs for other oxide glasses such as SiO_2 and GeO_2 [81].

[81] P. S. Salmon and A. Zeidler, Phys. Chem. Chem. Phys. **15**, 15286 (2013).

[82] A. Zeidler, P. S. Salmon, and L. B. Skinner, Proc. Natl. Acad. Sci. USA **111**, 10045 (2014).